Available online at www.sciencedirect.com

ScienceDirect

journal homepage: www.elsevier.com/locate/he

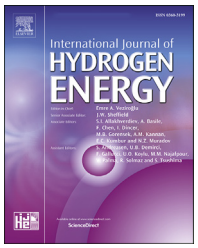

# 2D/2D Cu-tetrahydroxyquinone MOF/N-doped graphene heterojunction as photocatalyst for overall water splitting

*Horatiu Szalad, Andres Uscategui, Josep Albero*[**], *Hermenegildo García*[*]

*Instituto Universitario de Tecnología Química CSIC-UPV, Universitat Politècnica de València-Consejo Superior de Investigaciones Científicas, Universitat Politècnica de València, Avda. de los Naranjos s/n, 46022, Valencia (Spain)*

## HIGHLIGHTS

- A 2D Cu MOF with tetrahydroxyquinone linker (CuTHQ) has been synthesized.
- 2D/2D heterojunctions (CuTHQ/NG) of CuTHQ and N-doped graphene have been prepared.
- In contrast to its components, CuTHQ/NG promotes photocatalytic overall water splitting.
- Photo-induced charge separation confirms charge transfer within the heterojunction.
- CuTHQ/NG heterojunction stability was demonstrated in a 96 hç photocatalytic experiment.

## ARTICLE INFO

*Article history:*
Received 12 November 2022
Received in revised form
10 December 2022
Accepted 14 December 2022
Available online 3 January 2023

*Keywords:*
2D MOF
Graphene
Photocatalysis
Overall water splitting
Charge separation
Heterojunction

## ABSTRACT

A novel 2D/2D heterojunction (CuTHQ/NG) has been prepared by *in situ* growth of the 2D CuTHQ MOF on defective N-doped graphene (NG), and its photocatalytic activity for overall water splitting studied in detail. CuTHQ/NG heterojunction has demonstrated better photocatalytic activity (480 μmol/g) than the individual components (257 and 65 μmol/g for CuTHQ and NG, respectively) for $H_2$ evolution. Furthermore, unlike the individual components, the as-prepared 2D/2D CuTHQ/NG heterojunction promotes overall water splitting under simulated sunlight (164 μmol of $H_2$/g and 80 μmol of $O_2$/g). We have also studied the photo-induced charge separation and recombination reactions. Photocurrent measurements and emission quenching experiments have confirmed improved charge separation in the CuTHQ/NG heterojunction. Moreover, the charge recombination kinetics have been investigated with transient absorption spectroscopy. Electron/hole recombination in the heterojunction has been determined more than one order of magnitude slower (8.9 μs) than the mechanical mixture of CuTHQ and NG (0.35 μs). Finally, the photochemical stability of the 2D/2D heterojunction has been investigated performing a long-term (96 h) experiment, demonstrating near linear $H_2$ evolution along the irradiation time.



* *Corresponding author.*
** *Corresponding author.*
E-mail addresses: joalsan6@upvnet.upv.es (J. Albero), hgarcia@qim.upv.es (H. García).

https://doi.org/10.1016/j.ijhydene.2022.12.168

## Introduction

Photocatalysis is considered an appealing approach for Sunlight energy storage, by transformating solar light into chemicals, some of which can be used as fuels. The "*solar fuels*" accumulate solar energy to be delivered on-demand. In this context, $H_2$ obtained through solar photocatalysis is attracting increasing attention in the last years as energy vector [1,2]. $H_2$ is currently produced mainly by steam reforming, which generates $CO_2$ emissions and, being an energy-intensive and unsustainable process [3].

Photocatalytic reactions involve four fundamental steps: i) light absorption by a semiconducting material, ii) photo-induced charge separation, iii) charge migration to the particle surface, and iv) occurrence of redox reactions with substrate at the solid interface. Some of the major bottlenecks limiting the efficiency of the photocatalytic process are an inefficient photo-induced charge separation [4], together with a fast electron/hole recombination of the photogenerated charges [5]. Different strategies have been proposed for decreasing charge recombination increasing the efficiency of photo-induced charge separation in semiconductors, such as doping, co-catalysts loading or heterojunctions formation, among others [6]. Heterojunction formation has proved to be one of the most promising methods to favor charge separation [7]. In this regard, 2D/2D heterojunctions can provide additional advantages derived from the large interfacial contact of the two components compared to other heterojunctions and a shorter charge migration path which both factors can notably improve charge separation [8]. For instance, Zhang et al. reported a hierarchical sheet-on-sheet $ZnIn_2S_4$/g-$C_3N_4$ heterostructure as photocatalyst, exhibiting an increased photocatalytic activity compared to the individual counterparts and 14 μmol of $H_2$/h. The authors attributed this enhanced photoactivity to the efficient internal photo-induced $e^-/h^+$ transfer [9]. In a different example, Dong et al. reported a ternary heterostructure comprising ZnO/ZnS/g-$C_3N_4$, reaching 1205 μmol/g under irradiation [10]. This activity was attributed to a multistep charge transfer and effective $e^-/h^+$ separation in this heterojunction.

Graphene and derivatives have attracted considerable research interest in photocatalysis. Specifically, graphenes doped with heteroatoms or containing defects have been reported as additives in photocatalytic systems as well as active photocatalysts [11]. Among the features that justify the use of defective graphenes in photocatalysis, the most important ones are their high specific surface area, strong substrate adsorption, high mobility of charge carriers and the possibility of rational design of active sites. Graphenes are among of the most widely-used materials to form heterojunctions with semiconductors to enhance their photocatalytic activity. Combined with semiconductors in the appropriate proportion and the best interfacial configuration, graphenes increase charge separation due to their electron mobility. Considering their morphology, graphenes should be specially suited to form heterojunctions with 2D MOFs, since the aspect ratio should allow the largest interfacial contact between the two components with the minimal diffusion length, making easier electron transfer from the initial charge separation state in the 2D MOF to the graphene.

On the other hand, metal organic frameworks (MOF), a class of porous crystalline materials consisting of metal nodes coordinated to rigid, multipodal organic ligands, feature unique properties such as large surface area and porosity, high content of transition metals. The possibility to be designed and modified after synthesis makes MOFs very promising heterogeneous catalysts or photocatalysts [12]. More recently, 2D MOFs have also attracted remarkable attention. Unlike their 3D analogs, 2D MOFs exhibit special additional properties due to the ultrathin layer thickness, high aspect ratio, abundant exposed unsaturated metal sites and favorable mass transfer [13]. Similarly to other 2D materials, the properties of 2D MOFs can be tailored with thickness [14]. 2D MOFs with excellent dimension-dependent properties have been previously explored in energy storage and electrocatalysis, among other applications [15–17]. However, less attention has been paid to these materials in photocatalysis, probably due to their metallic behavior, which induces ultrafast $e^-/h^+$ recombination kinetics.

The use of 2D/2D heterojunctions of graphene and 2D MOFs has been previously explored in different applications such as gas adsorbers [18], thermoelectric properties [19] and energy storage [20–22]. However, less attention has been paid to the photocatalytic activity of these graphene/2D MOF heterojunctions and specially in their performance in the photocatalytic water splitting.

This manuscript reports the performance of a defective graphene/2D MOF heterostructure for photocatalytic $H_2$ production. N-doped graphene has been previously reported as a convenient photocatalysts for $H_2$ evolution, especially when fabricated from biomass wastes [23]. On the other hand, the 2D Cu tetrahydroxy-1,4-quinone (CuTHQ) MOF, has been studied in energy storage and electrocatalysis, due to its enhanced conductivity and electronic properties [24–26]. In this regard, previous examples have shown Cu-MOF containing 1,4-benzenedicarboxylic acid linkers and graphene oxide composite has previously demonstrated enhanced electrocatalytic properties and stability in hydrogen evolution reaction (HER) [27]. Alternatively, $NH_2$-MIL-125(Ti)/r-GO heterostructure was fabricated by Karthik et al. for photocatalytic $H_2$ evolution. This photocatalyst produced 91 μmol/g·h, while the photocatalytic activity of the $NH_2$-MIL-125(Ti) MOF was only of 7 μmol/g·h under the same conditions [28]. Similarly, UiO-66-$NH_2$ with 50 wt% of graphene has been reported to produce 41.4 mmol/g·h of $H_2$ when Pt was used as co-catalyst, TEOA as sacrificial agent and Erythrosine B dye as sensitizer [29]. In general, most of the MOFs and derivatives/graphene composites are modified by metal or metal oxide co-catalysts to increase their performance. To the best of our knowledge the photocatalytic activity for overall water splitting of 2D MOF/defective graphene heterojunctions has not been reported so far [30].

Herein, we have found an efficient photo-induced charge separation when N-doped graphene (NG) and the 2D CuTHQ MOF are in intimate contact forming a 2D/2D heterojunction, enhancing its photocatalytic activity by a factor higher than 2-fold for $H_2$ evolution and demonstrating overall water splitting. Moreover, this heterostructure has demonstrated to be stable in a 96 h photocatalytic reaction.

## Experimental section

### Materials preparation

NG was prepared in a tubular quartz oven by pyrolyzing commercial chitosan at 900 °C for 2 h with heating rate of 5 °C/min and Ar flow.

CuTHQ was synthetized following previous procedure [26]. 60 mg of tetrahydroxy quinone (THQ) and 110 mg of $Cu(NO_3)_2 \cdot 3H_2O$ were each dissolved separately in 20 mL of MiliQ water. In the solution containing the metal salt, 46 μL of ethylenediamine (EDA) were added, and subsequently, the THQ solution was dropwise incorporated. The obtained solution was stirred vigorously for 12 h in a lidded flask. The obtained dark blue crystals were thereafter recovered by filtration, washed with 1 L of water and 50 mL of acetone, and finally dried under vacuum at 60 °C.

THQ could be hazardous in case of skin or eye contact and toxic in case of ingestion or inhalation (H315, H319 and H335). Inflammation of the eye is characterized by redness, watering and itching. Skin inflammation is characterized by itching, scaling, reddening, or, occasionally, blistering. Information about carcinogenic, mutagenic or teratogenic effects is not available.

For the CuTHQ/NG heterojunctions preparation, NG was first dispersed in MiliQ water at different concentrations (1, 1.5, 2, 2.5 and 3 mg/mL) and exfoliated by ultrasounds for 90 min. $Cu(NO_3)_2 \cdot 3H_2O$, THQ and EDA solutions were dropwise added to the NG dispersions and stirred vigorously for 12 h. The obtained solids were recovered by filtration and washed with 1 L of water and 50 mL of acetone. Finally, the heterojunctions were dried under vacuum at 60 °C.

### Characterization

PXRD diffraction patterns were acquired through a Shimadzu XRD-7000 diffractometer employing a $Cu_{ka}$ irradiation source ($\lambda = 1.5418$ Å) operational at 40kw and 40 mA. All data acquisition was done with a scanning speed of 10°/min in the 2–90 range (2θ°). The PXRD pattern of CuTHQ was obtained from the crystallographic information previously deposited on CCDC [12]. The software employed for processing and acquiring the crystallographic information was Mercury 3.8.

The chemical composition of all samples was determined via combustion.

Chemical analysis employing a CHNS FISONS elemental analyzer. All DRS spectra were acquired via a Varian Cary 5000 spectrophotometer in the range 200–800 nm. ATR-FTIR spectra were acquired through a Bruker Tensor 27 instrument equipped with a diamond ATR accessory. Raman spectra were acquired via a Horiba Jobin Yvon-Labram HR UV–visible–NIR (200–1600 nm) Raman microscope spectrometer employing a 514 nm laser. XPS spectra were recorded through a SPECS spectrometer equipped with a Phoibos 150 MCD-9 detector. The nonmonochromatic X-Ray source composed of Al and Mg was operated at 200 W. Before data acquisition, the samples were evacuated at $10^{-9}$ mba in the spectrometer antechamber. The work function of the device was calibrated with Ag, Au and Cu resulting in a value 4.2440 eV. The measured intensity ratios of the components were obtained from the area of the corresponding peaks after nonlinear Shirley-type background subtraction and corrected by the transition function of the spectrometer. FESEM images were acquired by using a ZEISS GeminiSEM 500 apparatus. The samples were applied directly on the support and subsequently investigated. TEM images were recorded via a JEOL JEM 2100F microscope operating under an accelerating voltage of 200 kV. The samples were uniformly dispersed in an ethanol solution and subsequently dropcasted on Ni TEM grids which were allowed to dry at room temperature. The supported samples were thereafter investigated via the TEM microscope. AFM measurements were carried out through a Bruker Multimode 8 Nanoscope instrument with a vertical resolution of 3 Å and a horizontal resolution of 5 nm.

Transient absorption spectra were recorded using the forth harmonic of a Q switched Nd:YAG laser (Quantel Brilliant, 266 nm, 15 mJ/pulse, 7 ns fwhm) coupled to a mLFP-122 Luzchem miniaturized detection equipment. This transient absorption spectrometer includes a 300 W ceramic xenon lamp, 125 mm monochromator, Tektronix TDS-2001C digitizer, compact photomultiplier and power supply, cell holder and fiber-optic connectors, computer interfaces, and a software package developed in the LabVIEW environment from National Instruments. The laser flash generates a 5 V trigger pulses with programmable frequency and delay. The rise time of the detector/digitizer is~3 ns up to 300 MHz (2.5 GHz sampling). The monitoring beam is provided by a ceramic xenon lamp and delivered through fiber-optic cable. The laser pulse is probed by a fiber that synchronizes the photomultiplier detection system with the digitizer operating in the pre-trigger mode. For the photocurrentexperiments, the solid samples were foremost dispersed in an ethanol solution containing a commercial Nafion binder. The obtained slurry was thereafter dropcasted onto FTO glass and allowed to dry at room temperature.

All measurements employed an Ag/AgCl reference and a glassy carbon counter. The electrolyte used was a 0.1 M aqueous solution of KCl.

All photoelectrochemical data was acquired via a VersaStat 3 potentiostation.

### Photocatalytic tests

Photocatalytic water splitting was investigated upon irradiation of a 20 mg/mL solution containing the photocatalysts with a 150 W Xe Lamp (0.1 W/cm$^2$ intensity). The reaction vessel was made of quartz, and the internal pressure was assessed via a manometer attachment.

Analysis of the evolved gases has been carried out through a micro-GC with two columns (Molsieve 5 A and PorePlot Q) and TC detector that allowed us to monitor and quantify $H_2$, $O_2$, $CO_2$, among other gases.

## Results and discussion

### 2D/2D heterojunctions preparation and characterization

Three different CuTHQ/graphene heterojunctions having in common the 2D MOF CuTHQ and differing in the graphene

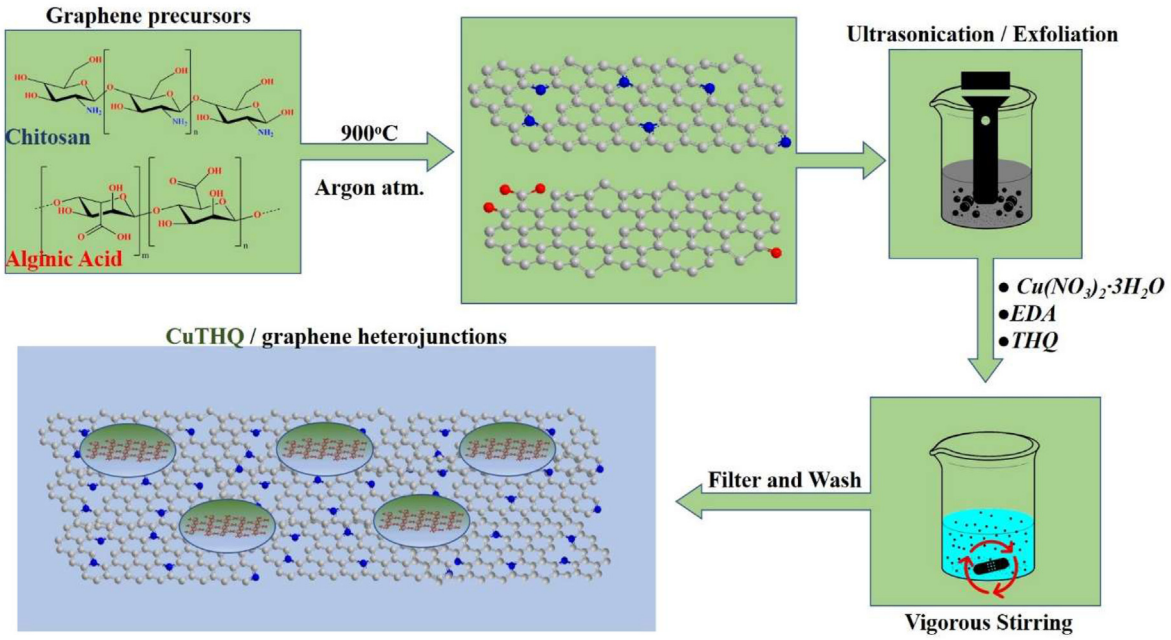


**Scheme 1 – Preparation procedure of CuTHQ/graphene heterojunctions, comprising graphene precursor pyrolysis, exfoliation, addition of CuTHQ precursors, and CuTHQ synthesis on graphene.**

materials were obtained. Samples preparation is illustrated in Scheme 1, and described in detail in Experimental Section. In brief, chitosan and alginic acid were pyrolyzed, following reported procedures, to obtain N and O-doped graphenes (NG and OG), respectively [31,32]. For comparison, a commercial sample of reduced graphene oxide (rGO) was also employed. The chemical composition of the different graphenes was determined by combustion elemental analysis (see Table 1). Then, the different graphenes were exfoliated by ultrasounds. Various graphene concentrations (1, 1.5, 2, 2.5 and 3 mg/mL) were used. The CuTHQ/graphene heterojunctions were finally prepared through a single step synthetic procedure in which, $Cu(NO_3)_2$ was first dissolved in the different graphene aqueous dispersions, followed by ethylenediamine (EDA) addition. Subsequently, THQ aqueous solution was dropwise added, and the final mixtures stirred for 12 h to afford the target CuTHQ/graphene heterojunctions. Table 1 summarizes the main analytical data of the samples under study. Depending on the initial graphene concentration in the aqueous dispersion, heterojunctions with different CuTHQ/graphene ratios were obtained (see Table 1).

For comparison purposes, the 2D CuTHQ MOF in the absence of graphene was also prepared, using a previously reported procedure [26]. Combustion chemical analysis of CuTHQ shows that the C, N, and O content of the synthetized MOF is close to the theoretical values of the ideal $[Cu_3(C_6O_6)_2(NH_3CH_2CH_2NH_3)_{1.5}]$ formula [25]. Moreover, the powder

**Table 1 – Summary of the main analytical data obtained from combustion elemental analysis and ICP-OES of the samples under study.**

| Samples | Elemental analysis (wt.%) | | | ICP-OES (wt.%) | | |
|---|---|---|---|---|---|---|
| | C | O | N | Cu | CuTHQ[a] | CuTHQ/graphene ratio |
| NG | 78.92 | 13.41 | 6.39 | – | – | – |
| OG | 71.92 | 27.28 | 0.25 | – | – | – |
| rGO | 91.06 | 8.24 | 0.54 | – | – | – |
| CuTHQ[b] | 30.79 | 30.23 | 5.28 | 31.12 | – | – |
| CuTHQ[c] | 29.20 | 31.10 | 6.80 | 31.00 | – | – |
| CuTHQ@rGO2 | 69.66 | 17.22 | 2.57 | 9.41 | 31.17 | 0.45 |
| CuTHQ@OG2 | 64.60 | 23.30 | 2.28 | 8.52 | 28.25 | 0.39 |
| CuTHQ@NG1 | 44.57 | 30.34 | 4.32 | 19.05 | 63.11 | 1.71 |
| CuTHQ@NG1.5 | 54.81 | 27.50 | 5.37 | 10.51 | 34.81 | 0.53 |
| CuTHQ@NG2 | 63.07 | 21.58 | 5.19 | 8.65 | 28.66 | 0.40 |
| CuTHQ@NG2.5 | 62.34 | 25.14 | 4.90 | 6.15 | 20.36 | 0.26 |
| CuTHQ@NG3 | 67.66 | 19.34 | 5.77 | 5.65 | 18.70 | 0.23 |

[a] Based on the MOF wt.% obtained from ICP-OES and the theoretical formula weight (619.62 g/mol) obtained from the cell formula $[Cu_3(C_6O_6)_2(NH_3CH_2CH_2NH_3)_{1.5}]$;
[b] Corresponds to the synthetized CuTHQ MOF;
[c] Obtained from the theoretical formula weight of the MOF (619.62 g/mol).

X-ray diffraction (PXRD) pattern of the synthetized CuTHQ MOF matches well with the simulated pattern (see Fig. S1 in Supporting Informations for the comparison of the experimental and simulated PXRD patterns), both in good agreement with previous reports [26], confirming the success in the CuTHQ MOF synthesis.

The PXRD patterns of NG, CuTHQ and the CuTHQ/NG2 heterojunctions are presented in Fig. 1 a. NG PXRD pattern presents a broad and low intensity peak at 26.5°, attributed to π-π layer stacking of graphene sheets. The characteristics PXRD peaks at 8°, 16°, 25° and 30° in CuTHQ [26] can be also observed in the CuTHQ/NG2 heterojuntion, suggesting that the 2D MOF have been formed in the presence of the NG sheets. It is worth commenting that most of the main crystal peaks from CuTHQ match with those of the CuTHQ/NG2 heterojunction. However, the peak at 25° in CuTHQ appears 0.4° shifted in CuTHQ/NG2, together with a new peak at 18°. This could be indicating that CuTHQ crystal structure suffers some distortion in contact with the N-doped G.

The formation of the CuTHQ/graphene heterojunctions is further evidenced by Fourier Transform-Infrared spectroscopy (FTIR) (Fig. 1 b). CuTHQ vibrational peaks at 558, 625, 784, 1016, 1048, 1085, 1345, 1474 and 1607 $cm^{-1}$ correlated to ν C–C skeleton vibration, ν C–CO–C in plane deformation, ν N–H deformation in EDA, ν C–N stretching in EDA, ν C–C skeleton vibration, ν C=O stretching, C–N stretching in EDA, ν C–H deformation in EDA and ν C=O stretching vibration, respectively, can also be observed in the heterojunction.

Raman spectra of NG, CuTHQ and CuTHQ/NG2 are presented as Fig. S2. As can be seen there, NG shows the typical 2D (2700 $cm^{-1}$), G (1580 $cm^{-1}$) and D (1350 $cm^{-1}$) bands characteristic of defective graphenes obtained from the pyrolysis of chitosan [31]. Alternatively, CuTHQ presents vibrational bands at 356.57 $cm^{-1}$, 432.98 $cm^{-1}$, 547.59 $cm^{-1}$, 713.14 $cm^{-1}$, 1235.27 $cm^{-1}$ and 1528.16 $cm^{-1}$, among others. The first three peaks in the low frequency region have been attributed to ν Cu–O in MOFs [33], while the three vibrational peaks at longer frequencies are assigned to C–C aliphatic chains, N–C–H rocking and C=O stretching, respectively. The CuTHQ/NG2 heterojunction Raman spectrum shows bands characteristics from both components. Thus, the characteristic 2D, G and D bands from defective graphene, together with the Raman shifts of Cu–O, C–C and C=O from the CuTHQ can be simultaneously observed. It is worth nothing that a new vibrational band located at 226.29 $cm^{-1}$ was also recorded, and it could be attributed to the Raman-active phonon modes of $Cu_2O$ [34].

X-ray photoelectron spectroscopy (XPS) analysis were also performed for NG, CuTHQ and the CuTHQ/NG2

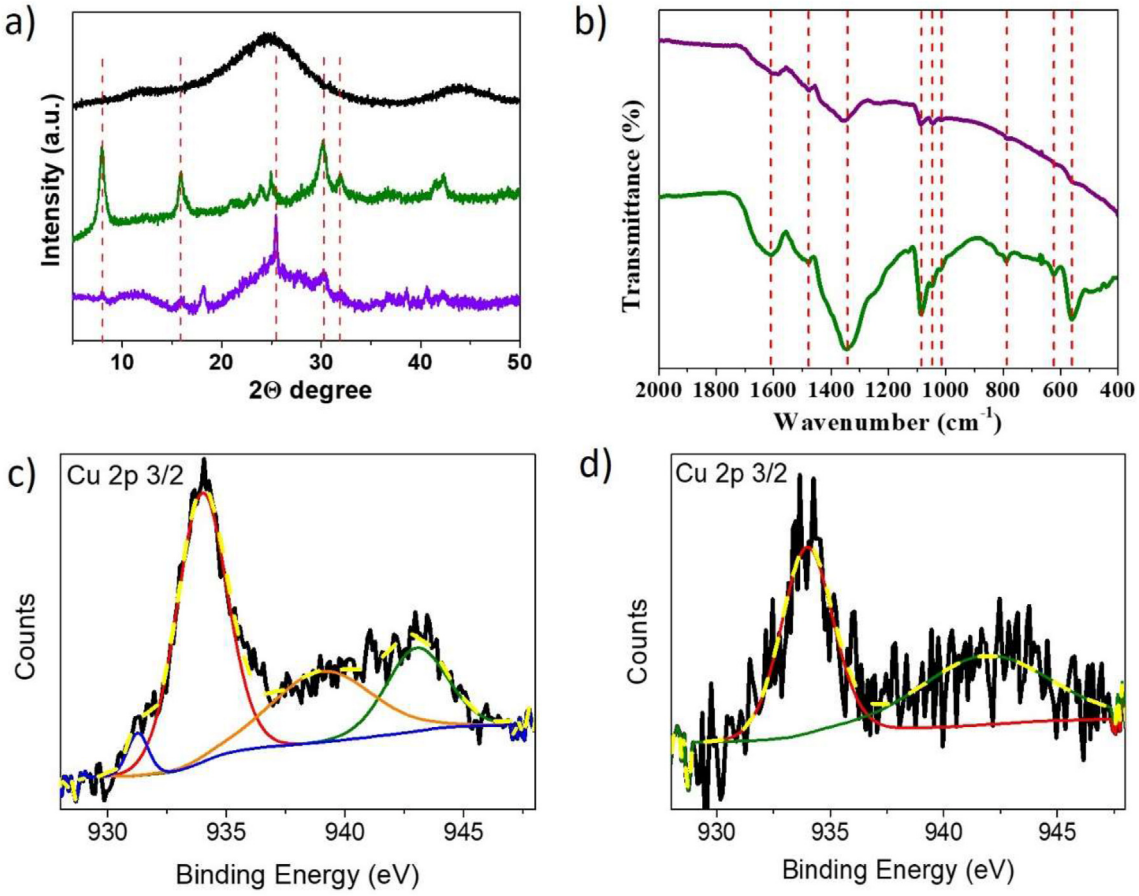


**Fig. 1 – (a) PXRD patterns of NG (black), CuTHQ (green) and the CuTHQ/NG2 heterojuntion (purple). (b) FTIR spectra of CuTHQ (green) and CuTHQ/NG2 heterojunctions (purple). Red, dashed lines indicate the main peaks. High-resolution peak Cu 2p 3/2 XPS of CuTHQ (c) and CuTHQ/NG2 (d) and the best fittings to individual components. (For interpretation of the references to colour in this figure legend, the reader is referred to the Web version of this article.)**

heterojunction. The high-resolution C 1s peak in NG shows the typical components of N-doped defective graphene (see Fig. S3) [31]. The main component is centred at 284.5 eV and it is attributed to $sp^2$ carbon atoms, while two other components at 286.1 eV and 289.4 eV can be assigned to C–O and O–C=O bonds, respectively. The high-resolution O 1s spectrum peak revealed two components at 530.7 and 533.1 eV, assigned to C=O and C–O bonds, respectively, in good agreement with the C 1s components. The N 1s spectrum shows two components (398.0 eV and 400.5 eV) that can be ascribed to pyridinic and quaternary N, respectively.

C 1s, O 1s and N 1s XPS measurements in the CuTHQ MOF were also recorded. They are presented in Fig. S4. The high-resolution C1s peak has been deconvoluted in three components at 284.5 eV, 286.1 and 288.2 eV, attributed to $sp^2$ C, and oxygenated C–O and C=O bonds, respectively. O 1s spectrum shows three components (532.6 eV, 531.5 eV and 530.6 eV) related to C–O, weakly oxygen species and Cu–O, respectively [35]. A small N 1s peak can be also observed in the CuTHQ XPS spectrum, as consequence of the presence of EDA in the synthetic procedure. Finally, the high-resolution Cu 2p 3/2 spectrum (Fig. 1 c) shows a main peak at 934.0 eV together with strong satellite peaks, indicating $Cu^{2+}$ as the main oxidation state in CuTHQ [24]. Additionally, the Cu 2P 2/3 has also a minor component at 931.2 eV that can be assigned to $Cu^{+}$ [25]. It is worth commenting that the strength and shape of shake-up satellites is typically used for assigning chemical states. In the present case, the strong shake up satellite in the Cu 2p 3/2 is characteristic of Cu(II) species such as $Cu(OH)_2$ and CuO, unlike Cu(I) species [36].

The Cu 2p 3/2 XPS spectrum of CuTHQ/NG2 heterojunction is also presented in Fig. 1 d. A main peak at 934.0 eV and its respective satellite peaks can still be appreciated despite Cu is present in lesser amount in the CuTHQ/NG2 heterojunction. Interestingly, the small component attributed to $Cu^{+}$could not be appreciated in CuTHQ/NG2.

Altogether, the available chemical characterization data suggests that CuTHQ MOF has been successfully synthetized in the presence of N-doped graphene.

The 2D morphology in the CuTHQ MOF was confirmed by high-resolution field-effect scanning electron microscopy (HRFESEM) and high-resolution transmission electron microscopy (HRTEM). As can be seen in Fig. 2, HRFESEM image of as-synthetized CuTHQ show a morphology characteristic in some 2D materials. The 2D morphology of CuTHQ after exfoliation was further confirmed by HRTEM (Fig. S5), in which images showing the stack of very crystalline and thin layers can be observed.

The morphology of CuTHQ/NG2 was also studied by HRFESEM (Fig. 2). The characteristic morphology previously observed in CuTHQ can still be seen in the heterojunction. However, the MOF sheets are embedded in a smooth matrix, corresponding to the N-doped graphene (Figs. S5 and SI), forming a heterogeneous composite. Elemental mapping of a representative CuTHQ/NG2 scanning transmission electron microscopy (STEM) image (Fig. 2 c–f) confirms the presence of Cu and O homogeneously distributed on the sample, while C can only be clearly observed in some regions.

Atomic force microscopy (AFM) images of NG, CuTHQ and CuTHQ/NG2 were also acquired, and they are presented in Fig. S6. As can be seen there, NG shows laminar morphology of approximately 3 nm thickness and a mean roughness square ($R_{mq}$) of 0.50 ± 0.15 nm. On the other hand, the CuTHQ layers present a lateral size of 4 nm, and a $R_{mq}$ of 0.20 ± 0.07 nm. Finally, CuTHQ/NG2 images show stacks of layers of different thickness. In selected images it can be seen that the thickness

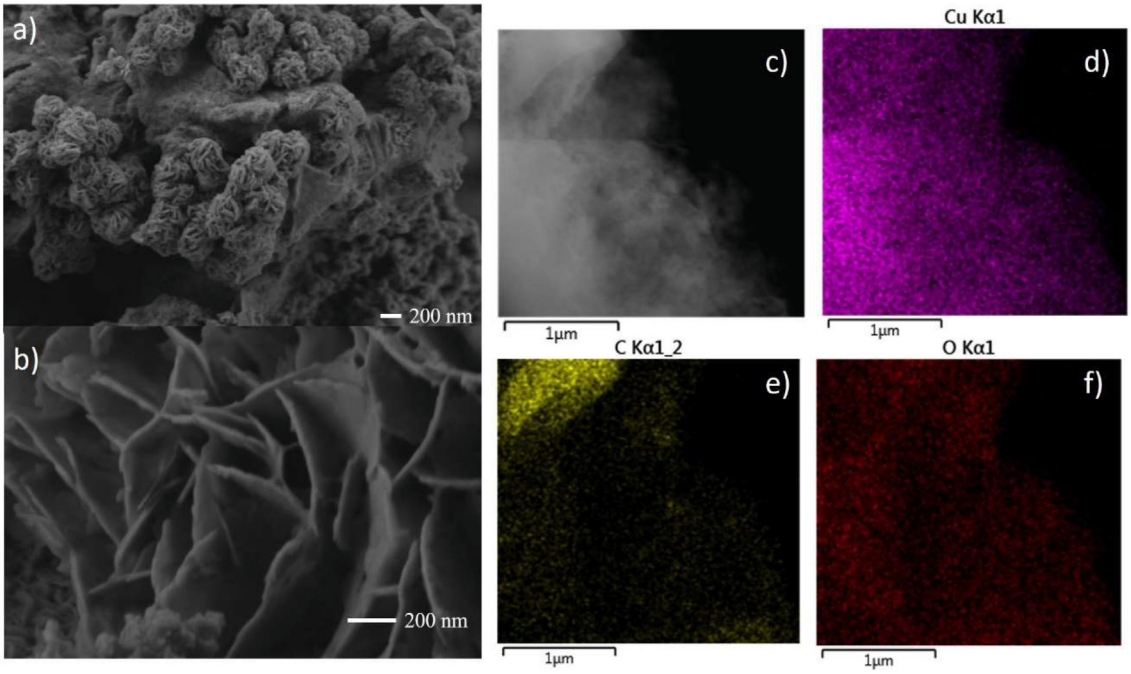


**Fig. 2 – HRFESEM images of CuTHQ@NG2 (a) and CuTHQ (b), and STEM image (c) and elemental mapping (d–f) of CuTHQ/NG2.**

of the bottom layer is of approximately 3 nm, while subsequent layers on top of the previous one are of 4 nm thick, approximately. In this case the $R_{mq}$ is of 0.23 ± 0.02 nm. This is suggesting that in CuTHQ/NG some NG and CuTHQ layers are intercalated, forming heterojunctions. Altogether, the available data suggest that the 2D CuTHQ MOF has been successfully formed on graphene sheets and both materials are forming a random MOF/graphene heterojunctions.

### *Photocatalytic activity*

The photocatalytic activity of the CuTHQ/graphene heterojunctions has been studied for $H_2$ evolution upon UV–vis light irradiation with a 150 W Xe lamp by dispersing 20 mg of the different heterojunctions in MilliQ water:MeOH (70:30, v:v) at 1 mg/mL, purging exhaustively with Ar before irradiation. Analysis of the gases ($H_2$, $O_2$, $N_2$, etc) was performed by connecting directly a home-made quartz photoreactor (see Fig. S7) to a micro-GC equipped with Molsieve 5 A column and TC detector.

The $H_2$ production after 24 h reaction from aqueous dispersions of CuTHQ/NG heterojunctions having different proportions of the two components (see Table 1) is shown in Fig. S8. Control experiments using NG and CuTHQ as photocatalysts have also been carried out. Under these conditions, the $H_2$ produced using CuTHQ/NG heterojunctions at different ratios was similar or higher than that of CuTHQ, depending on the MOF:graphene ratio, and in all cases larger than that of NG. A maximum $H_2$ production (480 μmol/g) was obtained using CuTHQ/NG2 (CuTHQ:NG ratio of 0.4) as photocatalyst. The $H_2$ evolution from CuTHQ and NG upon light irradiation at the same conditions were of 257 and 65 μmol/g, respectively. Additional control experiment in the dark, by covering the photoreactor with aluminum foil, while light was on, were also carried using CuTHQ/NG2, but undetectable $H_2$ evolution was measured.

Alternatively, the photocatalytic $H_2$ production using the different graphenes at the optimum ratio (CuTHQ/Graphene = 0.4) has also been investigated (Fig. 3). As can be observed, the $H_2$ production obtained using OG and rGO were very similar, and approximately half than that achieved for the NG heterojunction. This is indicating that N atoms doping graphene contributes favorably to the photocatalytic activity of these heterojunctions. This is not surprising since some precedents in the literature report the photocatalytic activity in defective graphenes arises from the presence of heteroatoms and lattice defects, which modify the electronic structure of graphene converting them into semiconductor materials [37].

For comparison purposes, NG and CuTHQ have been mechanically mixed in an Agata mortar in identical proportion as that of CuTHQ/NG2 heterojunction and dispersed in water:MeOH to evaluate the photocatalytic activity for $H_2$ production (Fig. 3 b). As can be observed, the CuTHQ and NG mixture showed approximately half of $H_2$ production than that exhibited by the heterojunction. This lower photocatalytic activity of the mechanical mixture indicates the benefits of the synthetic procedure for CuTHQ/defective graphene heterojunctions developed here to promote an intimate contact between these two materials, leading to better photocatalytic activity than the mechanical mixture of the independent materials. Therefore, the direct growth of 2D CuTHQ MOF on graphene sheets leads to an interfacial better overlap of the MOF-graphene facets that result on a more efficient charge separation between these materials, extending the lifetime of photogenerated charges and decreasing charge recombination.

The photocatalytic activity towards overall water splitting upon UV–Vis irradiation in the absence of MeOH as sacrificial electron donor was also tested (Fig. 3 c). As can be seen there, simultaneous production of $H_2$ and $O_2$ in stoichiometric amounts (164 μmol of $H_2$/g and 80 μmol of $O_2$/g) were measured for CuTHQ/NG2, while undetectable amounts of $H_2$ and $O_2$ could be obtained for CuTHQ and NG separately (data not shown). This is suggesting efficient charge separation in the heterojunction, while faster recombination kinetics from their individual components. It has been previously reported that some MOF can decompose during the oxygen evolution reaction (OER), especially in electrochemical OER, resulting in metal oxides [38,39]. However, FESEM and HRTEM images of CuTHQ/NG2 after overall water splitting revealed no noticeable changes in the particles after reaction, as can be seen in Fig. S9 in SI.

The spectral response of CuTHQ/NG2 heterojunction was also investigated. The UV–Vis diffuse reflectance spectra of NG, CuTHQ and CuTHQ/NG2 are shown as Fig. S10. NG shows the typical continuous absorption decreasing in intensity

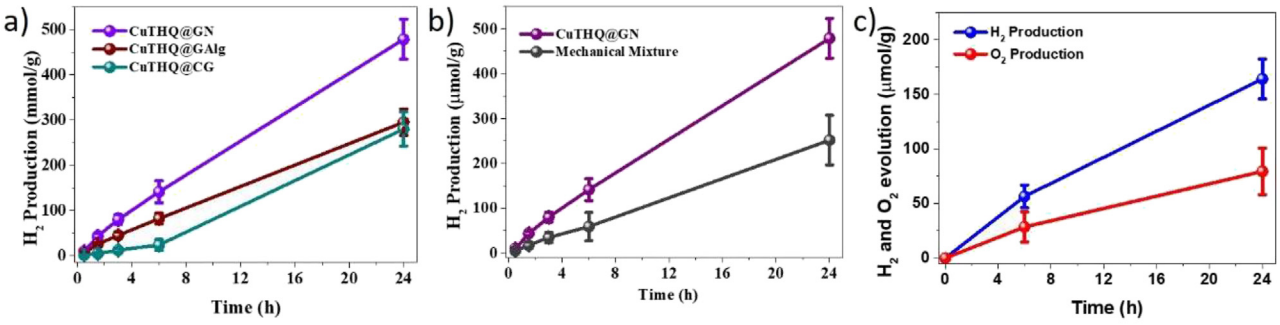


**Fig. 3 – $H_2$ production from CuTHQ/graphene heterojunctions using the different graphenes (NG, OG and rGO) (a). Comparison of the $H_2$ evolution from CuTHQ/NG2 and a mechanical mixture of NG and CuTHQ at the identical ratio than the heterojunction (b). Temporal evolution of $H_2$ and $O_2$ for CuTHQ/NG2 upon irradiation with a 150 W Xe lamp. Error bars indicate standard deviation obtained from three independent measurements.**

from the UV to the NIR already reported [31]. CuTHQ presents three broad absorption bands centred at 230 nm, 393 nm and 550 nm tailing in the NIR, as reported before [25]. The UV–vis diffuse reflectance spectrum of CuTHQ/NG2 is an additive combination of the two components and still shows these three characteristic bands from the 2D MOF. However, they are overlapped by a continuous absorption in the whole spectrum from the graphenic material. Surprisingly, despite the strong absorption in the visible and NIR regions, the $H_2$ evolution from CuTHQ/NG2 upon irradiation with the output of the Xe lamp filtered with a 360 nm cut-off filter was only of 24 μmol/g after 24 h illumination, as can be seen in Fig. S11, accounting only a 5% contribution from the visible region in the photocatalytic activity. This is indicating that mainly high energy UV photons are contributing to the photocatalytic $H_2$ production by CuTHQ/NG2 heterojunction, suggesting that it is benzoquinone excitation the component responsible for the photocatalytic activity.

In order to further investigate the spectral response of CuTHQ/NG2 as photocatalyst, the photoaction spectrum was determined by measuring the apparent quantum yield (AQY) using monochromatic light in the range from 200 to 600 nm (Fig. S12). As it can be seen there, CuTHQ/NG2 is mainly photocatalytically active in the UV region below 300 nm, exhibiting a maximum AQY of 1.6% at 225 nm, matching the CuTHQ absorption band centred at 230 nm. In comparison, this photocatalyst remain almost no active in the visible region. This photoresponse reinforces the proposal of THQ as the light harvesting unit triggering the photocatalytic overall water splitting.

Moreover, the photochemical stability of CuTHQ/NG2 heterojunction was investigated performing a long-term (96 h) photocatalytic experiment (Fig. S13 a). As can be observed there, near linear $H_2$ evolution have been obtained from CuTHQ/NG2 dispersion in water:MeOH (70:30, v:v) during 4 consecutive days. HRTEM image of this photocatalyst after 96 h reaction shows that the bi-dimensional morphology of this heterojunction has not undergo significant changes (Fig.S13 b). This is pointing the high stability of these heterojunction as photocatalysts under these reaction conditions.

### *Photo-induced charge transfer reactions*

In order to gain information on the interfacial charge transfer reactions in this 2D/2D heterojunction, photocurrent experiments were carried out first. For this, three photoelectrodes containing NG, CuTHQ and CuTHQ/NG2 were fabricated depositing identical amounts of these materials on fluorine-doped tin oxide (FTO) electrodes. The photoelectrode preparation is described in the experimental section and the results presented as Fig. 4. The measured photocurrent followed the same trend that the photocatalytic activity. CuTHQ exhibited slightly higher photocurrent than NG, in good agreement with the photocatalytic experiments. Notably, CuTHQ/NG2 exhibits a 2.4-fold photocurrent enhancement compared to CuTHQ, indicating that more charges can be extracted from the CuTHQ/NG2 heterojunction upon illumination than in CuTHQ and NG photoelectrodes.

The charge separation yield was estimated via time correlated single photon counting (TCSPC) measurements by comparison of the integral of the area under the emission decays of CuTHQ, CuTHQ/NG2 and the mechanical mixture of CuTHQ and NG at a 0.4 ratio, after excitation at 260 nm, while keeping the acquisition time constant (12 min) (Fig. 4 b). As can be seen, the emission of CuTHQ is efficiently quenched (83.1%) in the CuTHQ@NG2 heterojunction, while only a 54.4% of the emission of CuTHQ is quenched from the mechanical mixture, in good agreement with the photocatalytic data. The photoluminescence quenching in the heterojunction can be assigned to an efficient charge separation from the CuTHQ to NG in the heterojunction.

On the other hand, the charge recombination was studied by transient absorption spectroscopy (TAS) experiments upon 355 nm laser excitation. The transient absorption spectrum of CuTHQ/NG2 presents a continuous absorption from 400 to 800 nm (Fig. S14). The coincidence of the temporal profile of

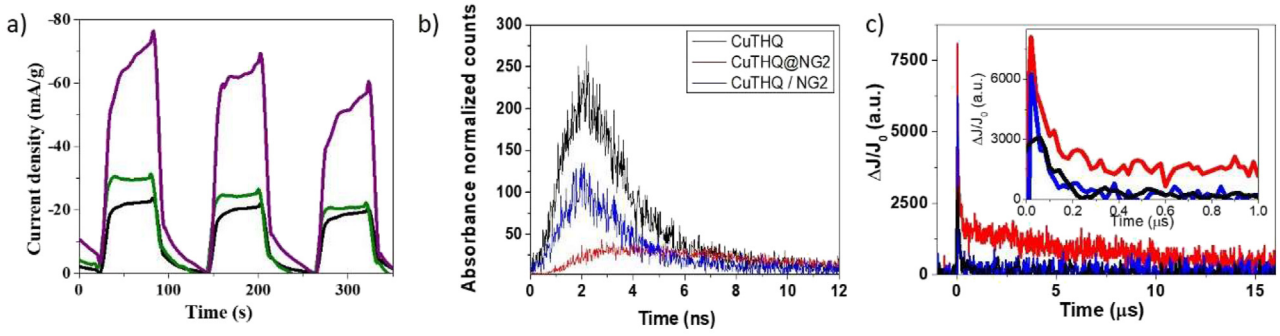


**Fig. 4 – (a) Photocurrent measurements of electrodes prepared by depositing CuTHQ/NG2 (purple), CuTHQ (green) and NG (black) on FTO electrodes (1.5 × 1 $cm^2$). Electrolyte: 0.1 M $LiClO_4$ in acetonitrile. Three consecutive cycles of 60 s were carried out switching on and off UV–vis light from a Xe lmap at 1080 $W/m^2$ irradiation while photocurrent values were acquired. (b) Emission decais of iso-absorbing, $N_2$-saturated dispersions of CuTHQ (black), CuTHQ@NG2 and a mixture of CuTHQ and NG at 0.4 ratio (blue) in acetonitrile upon 260 nm diode laser excitation. Time acquisition 12 min in all cases. (c) Transient absorption decays of CuTHQ/NG2 (black), CuTHQ (red) and the mechanical mixture of CuTHQ and NG at 0.4 ratio (blue) $N_2$-saturated dispersions in acetonitrile upon 355 nm laser excitation and monitored at 600 nm. Inset shows a zoom-in of the same plot at the initial time of the decay. (For interpretation of the references to colour in this figure legend, the reader is referred to the Web version of this article.)**

the transient decays monitored at different wavelengths confirm that this spectrum corresponds to a single transient species (Fig.S14 b). The decays can be adequately fitted to two consecutive decays, exhibiting a fast and a slow component of 64.9 ns and 8.9 μs (Equation (1)). The transient spectrum of CuTHQ has been also monitored in an acetonitrile dispersion upon 355 nm laser excitation (Fig. S14 a). Quenching experiments in $O_2$-saturated CuTHQ/NG2 dispersion in acetonitrile and $N_2$-saturated CuTHQ/NG2 dispersion in acetonitrile:MeOH (70:30, v:v) (Fig. S14 c) were carried out. The experimental data were fitted to Equation (1) and the slow components in both $O_2$-saturated and acetonitrile:MeOH exhibit shorter lifetimes of 5.5 μs and 4.4 μs, respectively, while the fast components did not presented significant changes (64.3 ns and 69.4 ns, respectively) probably reflecting the instrument response rather than the kinetics of the transients. The quenching behavior of the transient signal is indicating that the CuTHQ/NG2 transient spectrum presented in Fig. S14 a can be attributed to the simultaneous contribution of both $e^-$ and $h^+$ charge carriers.

$$f(t) = A_1 \cdot e^{-t/\tau 1} + A_2 \cdot e^{-t/\tau 2} \quad \text{(Equation 1)}$$

The transient absorption spectrum of CuTHQ has been also measured in $N_2$-saturated dispersion in acetonitrile (Fig. S14 a), exhibiting similar absorption characteristics than that of CuTHQ/NG2, but with lower signal intensity at faster lifetime (50 ns). Notably, CuTHQ does not show significant transient absorption in the μs time scale. Since both dispersions have been prepared at identical absorbance at the excitation wavelength (355 nm), the lower signal, especially at longer lifetime, can be assigned to a less efficient photo-induced charge separation in CuTHQ than in CuTHQ/NG2, in good agreement with the photocurrent experiments, emission decay quenching and the photocatalytic data. Moreover, a slower charge recombination is evidenced in the transient kinetics presented in Fig. 4 c. In this case, the experimental data from CuTHQ transient absorption kinetics can also be fitted to Equation (1). However, the obtained lifetime values for the fast and slow components are of 43.7 ns and 0.36 μs, respectively. For comparison purposes, the mechanical mixture of CuTHQ and NG at the optimum ratio (CuTHQ + NG2) has been also dispersed in $N_2$-saturated acetonitrile, and the transient kinetics measured (Fig. 4 c). As can be seen, the mechanical mixture of the CuTHQ MOF and NG exhibits faster recombination kinetics than the CuTHQ@NG2 heterojunction, and very similar to those of CuTHQ. The calculated lifetimes for CUTHQ + NGs from Equation (1) are 15.2 ns and 0.35 μs for the fast and slow components, respectively.

Therefore, the photocurrent, emission quenching and TAS measurements firmly confirm that the heterojunction between the CuTHQ MOF and NG enhances photo-induced charge separation efficiency, decreasing charge recombination. This is attributed to a better contact between these two materials as a result of the synthetic procedure in which the CuTHQ particles are grown on preformed NG. As evidence of this improved interface between these two materials, the mixture of these materials exhibits less efficient charge separation and faster recombination kinetics, in good agreement with the lower photocatalytic performance.

Most of the cases reporting MOF/graphene or derivative heterojunctions for photocatalytic $H_2$ evolution still require the use of noble metal co-catalysts to promote overall water splitting, to further favor the electron transfer between the MOFs and graphenic materials, increase the efficiency of charge separation and to slow down the recombination dynamics (see Table S1 in SI). However, in the present case, the favorable 2D/2D morphology of the MOF and defective graphene makes possible an intimate interfacial contact between these two materials, enhancing the yield of charge separation, and diminishing charge recombination rate. Thus, the 2D morphology not only results in an increase of the $H_2$ evolution using MeOH as sacrificial electron donor, but also promotes a substantial charge separation, which enables the simultaneous $H_2$ and $O_2$ evolution without the need of noble metal co-catalysts.

## Conclusion

The preparation procedure with *in-situ* growth and the 2D/2D morphology of the CuTHQ/NG heterojunction play a key role to achieve a large surface contact between the two components with a significant percentage of atoms in contact, and therefore a more efficient interfacial charge transfer. In this work, we have shown that Cu-THQ synthesized on N-doped graphene exhibits photocatalytic overall water splitting (164 μ mol of $H_2$/g and 80 μ mol of $O_2$/g) that is not observed for any of the two components separately or in much lesser extent for a mechanical mixture of the components. Charge extraction in photocurrent measurements is, in this way, higher for the *in situ grow* heterojunction than for each component. Also, transient absorption spectroscopy detects a longer-lived charge separation state in the heterojunction (8.9 μs) as compared to its components. In the negative site, it appears that the photocatalytic response derives from THQ ligand excitation ($\lambda < 360$ nm) and that other absorption bands recorded for Cu-THQ do not result in photocatalytic water splitting activity. This result points out to the key role of the ligand in the process and hints to further design of 2D MOFs with visible light harvesting ligands.

## Declaration of competing interest

The authors declare that they have no known competing financial interests or personal relationships that could have appeared to influence the work reported in this paper.

## Acknowledgment

Financial support by European Union – Next Generation EU, through the Conselleria de Innovación, Universidades, Ciencia y Sociedad Digital (GRAPHICA MFA/2022/023) and Generalitat Valenciana (Prometeo 2021-038) are gratefully acknowledged. This project has also received funding from the European Union's Horizon 2020 research and innovation programmes Solar2Chem, METHASOL and MOF2H2 under grant agreement No. 861151, No. 101022649, No. 101084131 respectively.

## Appendix A. Supplementary data

Supplementary data to this article can be found online at https://doi.org/10.1016/j.ijhydene.2022.12.168.

REFERENCES


[1] Hisatomi T, Domen K. Reaction systems for solar hydrogen production via water splitting with particulate semiconductor photocatalysts. Nature Catalysis 2019;2:387–99.

[2] Kim JH, Hansora D, Sharma P, Jang J-W, Lee JS. Toward practical solar hydrogen production – an artificial photosynthetic leaf-to-farm challenge. Chem Soc Rev 2019;48:1908–71.

[3] Chen S, Takata T, Domen K. Particulate photocatalysts for overall water splitting. Nat Rev Mater 2017;2:17050.

[4] Chen R, Fan F, Li C. Unraveling charge-separation mechanisms in photocatalyst particles by spatially resolved. Surface Photovoltage Techniques 2022;61:e202117567.

[5] Gao W, Lu J, Zhang S, Zhang X, Wang Z, Qin W, et al. Suppressing photoinduced charge recombination via the lorentz force in a photocatalytic system. Adv Sci 2019;6:1901244.

[6] Xu Y, Li A, Yao T, Ma C, Zhang X, Shah JH, et al. Strategies for efficient charge separation and transfer in. Artificial Photosynthesis of Solar Fuels 2017;10:4277–305.

[7] Low J, Yu J, Jaroniec M, Wageh S, Al-Ghamdi AA. Heterojunction photocatalysts. Adv Mater 2017;29:1601694.

[8] Su T, Hood ZD, Naguib M, Bai L, Luo S, Rouleau CM, et al. 2D/2D heterojunction of Ti3C2/g-C3N4 nanosheets for enhanced photocatalytic hydrogen evolution. Nanoscale 2019;11:8138–49.

[9] Zhang Z, Liu K, Feng Z, Bao Y, Dong B. Hierarchical sheet-on-sheet ZnIn2S4/g-C3N4 heterostructure with highly efficient photocatalytic H2 production based on photoinduced interfacial charge transfer. Sci Rep 2016;6:19221.

[10] Dong Z, Wu Y, Thirugnanam N, Li G. Double Z-scheme ZnO/ZnS/g-C3N4 ternary structure for efficient photocatalytic H2 production. Appl Surf Sci 2018;430:293–300.

[11] Albero J, Mateo D, García H. Graphene-Based materials as efficient photocatalysts for water splitting. Molecules 2019;24:906.

[12] Dhakshinamoorthy A, Li Z, Garcia H. Catalysis and photocatalysis by metal organic frameworks. Chem Soc Rev 2018;47:8134–72.

[13] Xue Y, Zhao G, Yang R, Chu F, Chen J, Wang L, et al. 2D metal–organic framework-based materials for electrocatalytic, photocatalytic and thermocatalytic applications. Nanoscale 2021;13:3911–36.

[14] Huang L, Zhang X, Han Y, Wang Q, Fang Y, Dong S. In situ synthesis of ultrathin metal–organic framework nanosheets: a new method for 2D metal-based nanoporous carbon electrocatalysts. J Mater Chem 2017;5:18610–7.

[15] Peng Y, Li Y, Ban Y, Yang W. Two-dimensional metal–organic framework. Nanosheets for Membrane-Based Gas Separation 2017;56:9757–61.

[16] Zhong H, Wang M, Chen G, Dong R, Feng X. Two-dimensional conjugated metal–organic frameworks for electrocatalysis: opportunities and challenges. ACS Nano 2022;16:1759–80.

[17] Zhao K, Zhu W, Liu S, Wei X, Ye G, Su Y, et al. Two-dimensional metal–organic frameworks and their derivatives for electrochemical energy storage and electrocatalysis. Nanoscale Adv 2020;2:536–62.

[18] Kumar R, Jayaramulu K, Maji TK, Rao CNR. Growth of 2D sheets of a MOF on graphene surfaces to yield composites with novel gas adsorption characteristics. Dalton Trans 2014;43:7383–6.

[19] Ninawe P, Gupta K, Ballav N. Chemically integrating a 2D metal–organic framework with 2D functionalized graphene. Inorg Chem 2021;60:19079–85.

[20] Jin J, Zhang Y-f, Wang H, Gong Y, Wang R, He B, et al. Rationally constructing a hierarchical two-dimensional NiCo metal–organic framework/graphene hybrid for highly efficient Li+ ion storage. Mater Chem Front 2021;5:4589–95.

[21] Beka LG, Bu X, Li X, Wang X, Han C, Liu W. A 2D metal–organic framework/reduced graphene oxide heterostructure for supercapacitor application. RSC Adv 2019;9:36123–35.

[22] Jayaramulu K, Dubal DP, Schneemann A, Ranc V, Perez-Reyes C, Stráská J, et al. Shape-assisted 2D MOF/graphene derived hybrids as exceptional lithium-ion battery electrodes. Adv Funct Mater 2019;29:1902539.

[23] Lavorato C, Primo A, Molinari R, Garcia H. N-doped graphene derived from biomass as a visible-light photocatalyst for hydrogen generation from water/methanol mixtures. Chem Eur J 2014;20:187–94.

[24] Majidi L, Ahmadiparidari A, Shan N, Misal SN, Kumar K, Huang Z, et al. 2D copper tetrahydroxyquinone conductive metal–organic framework for selective CO2 electrocatalysis at low overpotentials. Adv Mater 2021;33:2004393.

[25] Park J, Hinckley AC, Huang Z, Feng D, Yakovenko AA, Lee M, et al. Synthetic routes for a 2D semiconductive copper hexahydroxybenzene metal–organic framework. J Am Chem Soc 2018;140:14533–7.

[26] Jiang Q, Xiong P, Liu J, Xie Z, Wang Q, Yang X-Q, et al. A redox-active 2D metal–organic framework for efficient lithium storage with extraordinary high capacity. Angew Chem Int Ed 2020;59:5273–7.

[27] Jahan M, Liu Z, Loh KP. A graphene oxide and copper-centered metal organic framework composite as a tri-functional catalyst for HER. OER, and ORR 2013;23:5363–72.

[28] Karthik P, Vinoth R, Zhang P, Choi W, Balaraman E, Neppolian B. $\pi$–$\pi$ interaction between metal–organic framework and reduced graphene oxide for visible-light photocatalytic H2 production. ACS Appl Energy Mater 2018;1:1913–23.

[29] Wang Y, Yu Y, Li R, Liu H, Zhang W, Ling L, et al. Hydrogen production with ultrahigh efficiency under visible light by graphene well-wrapped UiO-66-NH2 octahedrons. J Mater Chem 2017;5:20136–40.

[30] Wang Z, Huang J, Mao J, Guo Q, Chen Z, Lai Y. Metal–organic frameworks and their derivatives with graphene composites: preparation and applications in electrocatalysis and photocatalysis. J Mater Chem 2020;8:2934–61.

[31] Primo A, Atienzar P, Sanchez E, Delgado JM, García H. From biomass wastes to large-area, high-quality, N-doped graphene: catalyst-free carbonization of chitosan coatings on arbitrary substrates. Chem Commun 2012;48:9254–6.

[32] Trandafir M-M, Florea M, Neaţu F, Primo A, Parvulescu VI, García H. Graphene from alginate pyrolysis as a metal-free catalyst for hydrogenation of nitro compounds. ChemSusChem 2016;9:1565–9.

[33] Dhumal NR, Singh MP, Anderson JA, Kiefer J, Kim HJ. Molecular interactions of a Cu-based metal–organic framework with a confined imidazolium-based ionic liquid: a combined density functional theory and experimental vibrational spectroscopy study. J Phys Chem C 2016;120:3295–304.

[34] Zhou J, Zhang Y, Wu G, Mao D, Lu G. Influence of the component interaction over Cu/ZrO2 catalysts induced with fractionated precipitation method on the catalytic

performance for methanol steam reforming. RSC Adv 2016;6:30176–83.
[35] Zhang K, Suh JM, Lee TH, Cha JH, Choi J-W, Jang HW, et al. Copper oxide–graphene oxide nanocomposite: efficient catalyst for hydrogenation of nitroaromatics in water. Nano Convergence 2019;6:6.
[36] de Groot F, Kotani A. Core level spectroscopy of solids. CRC Press; 2008.
[37] Mateo D, García-Mulero A, Albero J, García H. N-doped defective graphene decorated by strontium titanate as efficient photocatalyst for overall water splitting. Appl Catal B Environ 2019;252:111–9.
[38] Zheng F, Xiang D, Li P, Zhang Z, Du C, Zhuang Z, et al. Highly conductive bimetallic Ni–Fe metal organic framework as a novel electrocatalyst for water oxidation. ACS Sustainable Chem Eng 2019;7:9743–9.
[39] Salmanion M, Najafpour MM. Structural changes of a NiFe-based metal-organic framework during the oxygen-evolution reaction under alkaline conditions. Int J Hydrogen Energy 2021;46:19245–53.